Micromechanical Modeling of Corroded Steel Joints Under Excessive Plastic Deformations

Mohammad Ali Mahdavipour[1], Dmitry Vysochinskiy[2]

[1] Ph.D. Research Fellow, Department of Engineering Sciences, University of Agder, Jon Lilletuns vei 9, 4879, Grimstad, Norway, Email: ali.mahdavipour@uia.no

[2]Associate Professor, Department of Engineering Sciences, University of Agder, Jon Lilletuns vei 9, 4879, Grimstad, Norway, Email: dmitry.vysochinskiy@uia.no

Abstract

Under excessive plastic deformations, pitting corrosion can accelerate ductile fracture initiation in steel structures. For an accurate numerical prediction of ductile fracture in corrosion pits, a micromechanical fracture criterion along with a fine three-dimensional solid meshing is required. Previous studies on this topic are limited to simple plates; however, for a more detailed component, e.g., steel beam-to-column joint, implementing the pit geometry on the global model of the joint is challenging in terms of meshing and computational time. In this paper, two-level numerical modeling was employed to reduce the complexity of the problem. In this technique, submodels with refined mesh are used to perform micromechanical simulations and assess the ductility degradation of joints. For a case study joint, it was found that the pits near the edge of the web and flange plates are the most critical and can reduce the fracture initiation displacement of the joint by about 25%. On the other hand, the pits located on the edges of plates or far from the edges caused a negligible reduction in the fracture initiation displacement of the joint. These results suggest two-level numerical modeling as a viable technique to facilitate micromechanical simulation of pitting corrosion in corroded steel joints.

KEYWORDS

Ductile fracture; corrosion pit; steel joint; void growth model; plastic deformation; submodeling

1. Introduction

Progressive collapse is defined as an unpredicted extreme situation in which a local failure leads to a disproportionate global or partial collapse of a structure (Adam et al. 2018; GSA 2016; Sadek et al. 2010). In frame structures, columns carry the most gravity loads, and their removal is the most critical progressive collapse scenario (Adam et al. 2018; GSA 2016; Sadek et al. 2010). In steel structures, the unbalanced loads due to column removal are transferred by alternative paths provided by adjacent beams and joints (Sadek et al. 2010). These components are supposed to develop shear, flexural, and catenary resisting actions until the system reaches a new equilibrium (Adam et al. 2018; Sadek et al. 2010). Therefore, they are normally designed and constructed so that critical zones (i.e., plastic hinges) can sustain excessive plastic deformations before the loss of integrity. As also observed in experiments (Lew et al. 2013; Wang et al. 2021), the ductile fracture is the main failure mode of joints under this loading scenario. To ensure sufficient ductility of steel components, design codes (AISC 2016a; AISC 2016b) define protected zones and requirements to avoid pre-existing notches on them. A notch located in a protected zone can cause stress and strain concentration and accelerate fracture in a local spot. Despite codes requirements, notches can also appear due to pitting corrosion under an aggressive environment. Pitting corrosion is one of the main forms of corrosion that initiates and propagates locally in steel structures located in a corrosive environment (Bardal 2004; Pedeferri 2018). Various structures, including industrial steel structures located in coastal areas, LPG terminals located on jetties, topsides of offshore facilities, can be subjected to pitting corrosion. These corroded structures can also experience extreme events like a column removal due to a ship or vehicle collision (see Fig. 1), a localized fire, an explosion caused in industrial facilities by gas pipe fracture, or a leakage of combustible liquids (Adam et al. 2018). The collapse of these facilities must be investigated under the coupled effect of the pitting corrosion and excessive plastic deformations to avoid disasters in terms of casualties, economy, and environment (DNV GL 2015).

In general, the location of pits is extremely stochastic and difficult to predict (Bardal 2004; Pedeferri 2018). In addition, localized penetration and high cathodic to anodic area ratio increase the penetration speed so that pitting corrosion can affect a large portion of metal thickness in a short time (Pedeferri 2018). Depending on the geometry of pits, they can increase the plastic strain and stress

triaxiality (Cerit 2013; Cerit et al. 2009; Ji et al. 2015; Pidaparti and Patel 2008; Turnbull et al. 2010; Wang et al. 2018) that are known as two influential parameters for ductile fracture initiation in metals (McClintock 1968; Rice and Tracey 1969). Ductile fracture initiation at the root or wall of a corrosion pit can be followed by ductile tearing that pushes the crack front at high-stress levels and increases the chance of failure by cleavage fracture and unstable crack propagation (Petti and Dodds Jr 2005; Wang et al. 2018). In most cases, no adequate information is available on the effect of localized corrosion on overall member ductility. Therefore, finite element analysis (FEA) is usually performed (International Standards Organization 2008). Previous studies on simple tensile plates (Ahmmad and Sumi 2010; Songbo et al. 2021; Wang et al. 2018; Wang et al. 2017; Xu et al. 2016; Zhao et al. 2020) indicated that when the ductile fracture of steel components is under investigation, a three-dimensional representation of the pit geometry associated with a micromechanical fracture criterion is needed to assess the structural integrity. A fine discretization of the corrosion geometry must be utilized in such numerical models to predict the local responses on the pits properly (Ahmmad and Sumi 2010; Songbo et al. 2021; Wang et al. 2018; Wang et al. 2017). However, to the authors' knowledge, no study has quantified the effect of pitting corrosion on the ductility of steel joints under a column removal scenario. Steel joints possess more sophisticated geometries than simple plates and can produce more complicated stress and strain distributions. The solid meshing of the complex geometry of a joint and analyzing it for various pitting scenarios could be challenging, particularly when a micromechanical fracture criterion is employed. In addition, multiple zones in joints can experience excessive plastic deformations that all must be investigated for fracture.

This study aims to reduce the difficulties regarding meshing and micromechanical simulation of the corroded joints using a two-level numerical modeling technique. This technique was used through a parametric numerical study to assess the effect of an isolated corrosion pit on the ductile fracture initiation of a case study joint. Based on such analyses, one can determine which pit (with a certain geometry and location) can be considered critical and must be treated to avoid joint collapse for probable future events.

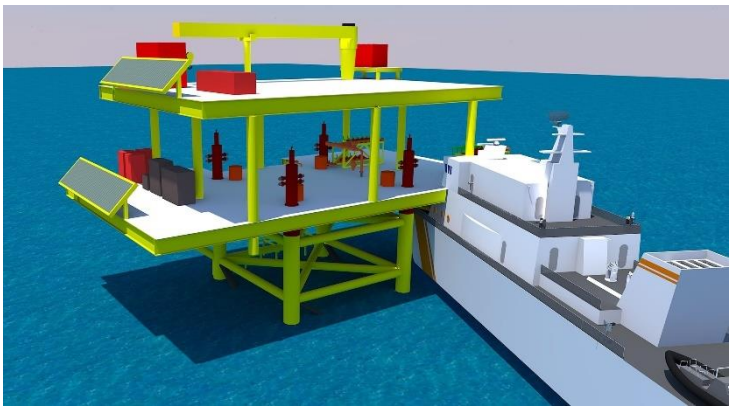

Fig. 1. A collision between a vessel and a steel production platform can lead to a progressive collapse.

2. Methodology

When the ductile fracture is the failure mode of steel components, micromechanical fracture modeling predicts fracture more accurately than traditional fracture mechanics (Wang et al. 2011). Micromechanical models are able to simulate the fundamental mechanisms of fracture by utilizing the modern computational capacity to predict localized stresses and strains (Kanvinde and Deierlein 2004). However, when a notch like a corrosion pit exists, these models require fine solid meshing around the pit domain to accurately capture localized stresses and strains (Ahmmad and Sumi 2010; Songbo et al. 2021; Wang et al. 2018; Wang et al. 2017; Xu et al. 2016; Zhao et al. 2020).

On the other hand, the meshing convergence and computational time would be challenging if the overall three-dimensional model of a steel component (e.g., a joint) is used to implement pits. One possibility to refine the mesh in the pit domain is to use tetrahedral elements that support fully automatic tetrahedral meshers (Dassault Systèmes 2014). However, for the same degree of freedom and the same amount of layers of elements through the thickness of a member, one needs significantly more tetrahedral elements compared to hexahedrons (Wang et al. 2017). Moreover, the first-order tetrahedral elements are not sufficiently accurate for structural calculations, particularly when large plastic strains are involved (Dassault Systèmes 2014). As a result, the second-order formulation must be chosen that even needs more computational resources. In contrast, developed reduced integration hexahedral elements can remarkably increase computational efficiency without significant loss of accuracy (Dassault Systèmes 2014). Finally, it is worth mentioning that before fracture initiation, modeling details of a local region around the pit has a negligible effect on the overall solution of the joint.

This study utilized two-level numerical modeling to overcome difficulties associated with modeling pits in complicated geometries. First, as described in Fig. 2, the nonlinear finite element analysis of the joint (not corroded) is carried out at the global level without pit implementation. Then based on the outcomes of this model and submodeling technique, critical regions are studied for fracture modeling and pit existence. Submodeling is a technique to investigate a local region with a more refined mesh based on the interpolation of the solution from a relatively coarse mesh in the global model (Hirai et al. 1984; Kardak 2015; Mao and Sun 1991; Marenić et al. 2010; Narvydas and Puodziuniene 2014). This technique effectively obtains the solution with a higher resolution in the local region of interest, e.g., a corrosion pit (Liu et al. 2021; Mao and Sun 1991; Verma et al. 2019).

There are two common submodeling techniques. In the displacement-based method, the boundary conditions of the submodel are nodal displacements extracted from the global model. The second method is called stress-based submodeling that stresses or tractions from the integration points are transmitted to the submodel as boundary conditions. The displacement-based submodeling method is preferred for large displacement problems because boundary conditions calculated using displacement can converge faster than the stress field (Sun and Mao 1988). In addition, Narvydas and Puodziuniene (2014) demonstrated that displacement-based submodeling is less sensitive to the mesh density of the global model and can provide higher accuracy than the stress-based method.

Like other finite element methods, this technique is also subjected to numerical errors classified into two main categories: Discretization errors and boundary condition errors. Discretization errors are inherent in the determination of responses with the finite element method (Oñate 2013). Since using a fine mesh in submodels is controlled by micromechanical modeling, the discretization errors in the submodels might be less critical. As a result, most of the discretization errors are originated from the global model and must be kept within a reasonable range to calculate boundary responses accurately for the submodels (Kardak 2015). This error can be controlled by refining the mesh until further refinement causes no significant change in the nodal displacement output of the global model (Kardak 2015; Oñate 2013).

Besides the discretization errors, the submodeling technique is also affected by boundary condition errors (Cormier et al. 1999; Kardak 2015; Mao and Sun 1992). As illustrated in Fig. 2, mesh refinement in submodels creates additional degrees

of freedom at boundaries that do not exist in the global model (Sun and Mao 1988). The global solution only provides displacements at the nodes of the original coarse mesh. Consequently, the displacement boundary conditions for new nodes in submodels must be derived based on the shape function of the original elements in the global model (Sun and Mao 1988). This interpolation can induce error in the boundary condition of the submodels. Therefore, the global mesh size adequacy must be checked for proper transmission of displacements into submodels. In order to evaluate the amount of these errors, the boundary responses of the submodels are compared to the corresponding region in the global model. In addition, to reduce the effect of the boundary condition errors on the local notch, the submodel region must be sufficiently taken away from the region of interest. Sun and Mao (1988) suggested this distance at least one coarse element in the global model.

It is worth mentioning that submodeling is a one-directional boundary condition exchanging from the global to the submodel with no feedback from the submodel to the global model (Mora et al. 2020; Narvydas and Puodziuniene 2014; Verma et al. 2019). Therefore, for the displacement-based submodeling, it is essential to ensure that the stiffness of the submodel is the same as the corresponding region in the global model (Narvydas and Puodziuniene 2014). However, the stiffness can be different due to mesh refinement if the global mesh is significantly coarser than the submodel. In addition, when the fracture is under investigation, the stiffness of the submodel changes due to fracture development and material separation. In consequence, boundary conditions provided by the global model are not realistic for the post-fracture analysis of the submodel.

Since this study is limited to fracture initiation in joints, the submodel stiffness is not affected by local fracture propagation. Therefore, displacement-based solid-to-solid submodeling was considered to transmit the nodal displacements from the global model to the submodels as boundary conditions. Based on this technique and the procedure described in Fig. 2, various pit location scenarios were analyzed for a case study joint. Then, the fracture initiation displacement of each corroded scenario was compared with the intact submodel as a benchmark to quantify the joint degradation in terms of fracture initiation.

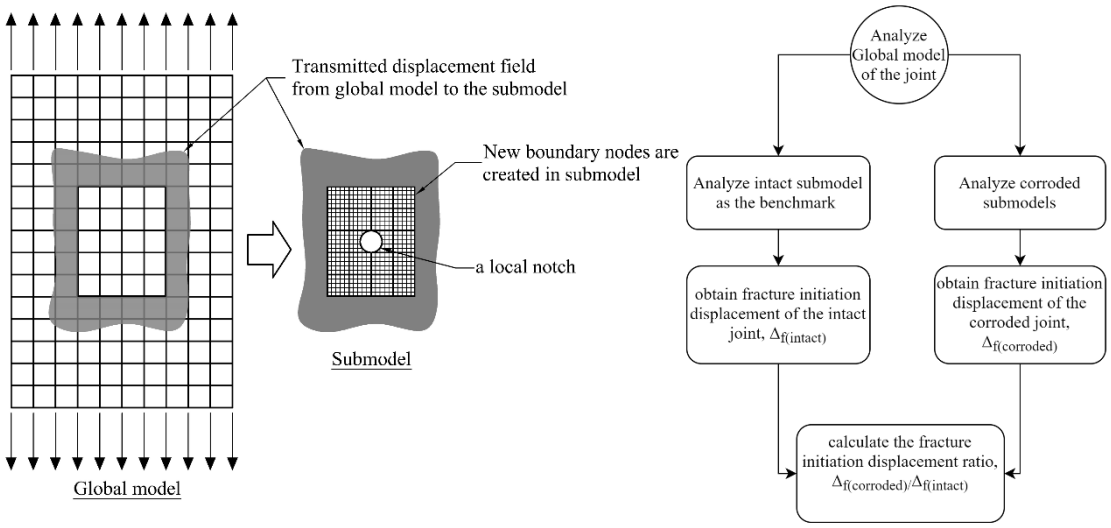

Fig. 2. An illustration of two-level finite element modeling and the procedure for micromechanical modeling of the corroded joints.

2.1. Micromechanical fracture criterion

Calibrated material constitutive model and fracture criterion are required to predict the nonlinear behavior and fracture initiation in steel material. In this study, the void growth model (VGM) was selected to characterize the ductile fracture initiation. Based on the theoretical studies done by Rice and Tracey (1969) on the processes of void growth and coalescence, Kanvinde and Deierlein (2006) used VGM as a micromechanical fracture criterion. In VGM, an explicit continuous integration of the stress triaxiality ratio (η) with respect to equivalent plastic strain ($\bar{\varepsilon}_p$) is done. These two parameters are known as the main influential parameters on the ductile fracture of metals under monotonic tensile loads (i.e., $\eta > 0.33$) (McClintock 1968; Rice and Tracey 1969). For situations with large geometry or triaxiality variation, VGM is a more appropriate criterion than instantaneous criteria in which only the current values of stress and strain are used (Kanvinde and Deierlein 2004). VGM has only one calibration parameter, i.e., the critical void growth index. Therefore, the model offers a good compromise between accuracy and complexity compared to other models like Gurson-Tvergaard-Needleman (GTN) with more parameters for a single material (Jia and Ge 2019).

Based on the VGM, the fracture initiates when the size of voids exceeds a critical value (Kanvinde and Deierlein 2006) that can mathematically be written as follows:

$$VGI = \int_0^{\bar{\varepsilon}_p} e^{1.5\eta}.\, d\bar{\varepsilon}_p > VGI_{critical} \qquad (1)$$

The left-hand side of this inequality is known as the Void Growth Index (VGI) that is an integration of η with respect to $\bar{\varepsilon}_p$. The critical void growth index ($VGI_{critical}$) on the right-hand side can be understood as a material property that is calibrated based on the smooth-notched tensile specimens and complementary finite element analyses (Kanvinde and Deierlein 2006). It is worth mentioning that to evaluate the fractured state based on a representative volume rather than a single point; the VGI is typically compared with $VGI_{critical}$ over a characteristic length (ℓ^*) of the mild steel that is reported 0.4-0.1 mm (Kanvinde and Deierlein 2006; Liao et al. 2012).

3. Case study

To present a demonstration of the described method, a sub-assemblage of a typical welded beam-to-column steel joint with an isolated corrosion pit was investigated under a column removal scenario. More details about this case study are presented in the following subsections.

3.1. Sub-assemblage description

As described in Fig. 3, the sub-assemblage was composed of two half-span beams and one column which moves vertically in the middle. This configuration has been widely used in different numerical and experimental studies (Adam et al. 2018) to simulate the effect of interior column removal. Based on this configuration, the inflection points are assumed at the middle of the beam span and modeled as pin supports (See Fig. 3).

A Welded Unreinforced Flange-Welded web (WUF-W) joint was selected in which rolled IPE360 steel beams were framed into a HE200M column by double-beveled tee welds and extra fillet welds as described in Fig. 4. Studies showed that adding an extra fillet weld effectively reduces fracture potential in the butt welds in moment-resisting joints (Chi et al. 2000). This weld configuration was selected to ensure that the weld is well-reinforced and does not fracture before the base metal, as the fracture of welds is outside the scope of this study. All steel members were fabricated from S355J2 steel grade that is known as a variant of S355 absorbing a minimum of 27J of energy in low temperatures (-20°C) based on the V-notch impact tests (European Committee for Standardization 2004). Weld access holes were used to perform the welds based on AWS D1.8, 2016 recommendation (American Welding Society (AWS) D1 Committee on Structural

Welding 2016). Fig. 4 illustrates the geometry of the weld access holes and continuity plates used in the studied joint.

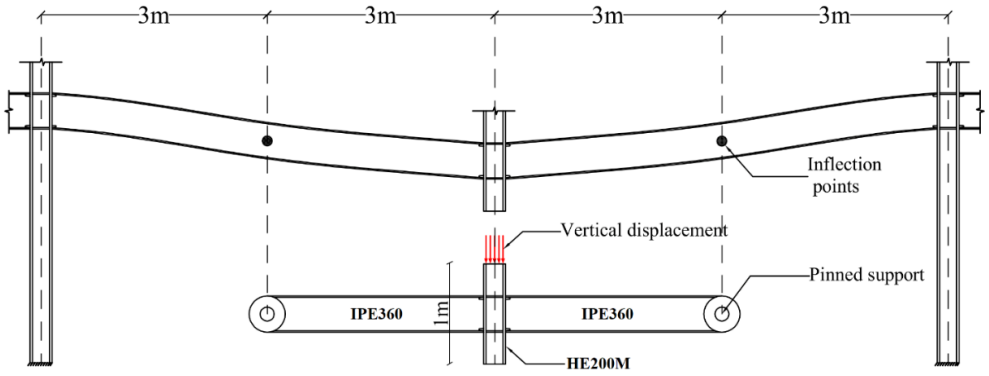

Fig. 3. The configuration of joint sub-assemblage under a column removal scenario.

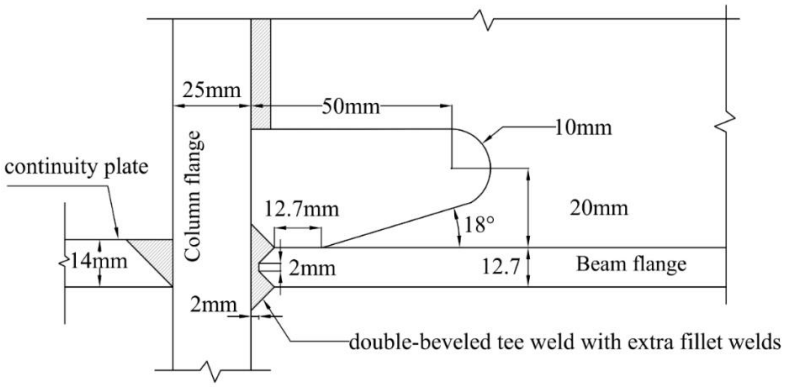

Fig. 4. Welding configuration and the weld access hole geometry of the studied joint.

3.2. Pit characteristics

Previous studies on corrosion pits (Duddu 2014; Xu et al. 2016) indicated that when they are significantly developed into the thickness of plates, the pits can be approximated by a semi-ellipsoid, as shown in Fig. 5. Many authors (Cerit 2013; Cerit et al. 2009; Huang et al. 2010; Wang et al. 2018; Yan et al. 2019; Zhang et al. 2015; Zhao et al. 2020) implemented pitting corrosion in numerical models based on this approximation. In this study, also a semi-ellipsoidal shape was assumed to be an acceptable morphology to implement pits in numerical models. Other possible pit geometries like narrow crack-shaped pits that increase the chance of brittle fracture were not considered in this research.

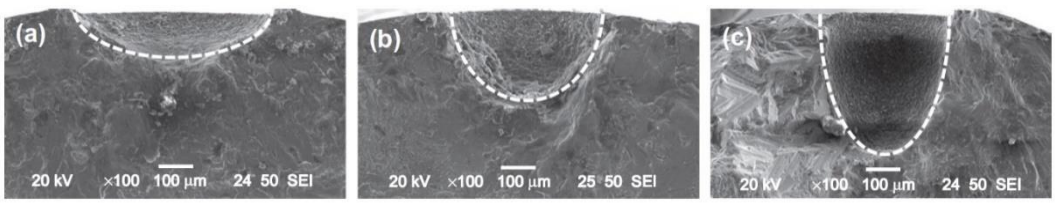

Fig. 5. Typical morphology of corrosion pits obtained by Scanning Electron Microscope (SEM) (Cerit 2013, with permission): (a) a wide semi-ellipsoidal pit, (b) a semi-spherical pit, and (c) a narrow semi-ellipsoidal pit.

The joint was studied for different scenarios of a single pit penetrated in critical regions of the described joint. According to Table 1, all pit scenarios can be classified into three categories based on the pit location relative to the free edge of the web or flange plate. In the edge pit category, the pit cut the free edge of the plates, and it was assumed that the pit center coincides with the edge line. In the near-edge category, the pit penetrates close to the free edge of the plates so that a ligament is formed between the pit and the edge. In this category, the effect of edge ligament was studied for three different ligament lengths ($l_e = t/12, t/6,$ and $t/4$), where t is the plate thickness. The rest of the pit scenarios are in the far-edge category in which the pit is located far from the free edges of the plates.

All these pit categories were also investigated for different geometrical parameters. According to Table 1, two values of pit depth were studied in which the pit penetrated to 50% and 25% of plate thickness (t). The plate thickness was 12.7 mm and 8 mm for the flange and the web of the beam (IPE360), respectively. In addition, for each depth, three different pit aspect ratios ($AR = 1, 0.5, 0.25$) were studied. This geometrical parameter is defined as the ratio between the pit radius and the pit depth ($AR = r/d$) and can affect local responses in the pit, i.e., plastic strain and stress triaxiality (Cerit 2013; Cerit et al. 2009; Ji et al. 2015; Pidaparti and Patel 2008; Turnbull et al. 2010; Wang et al. 2018). According to this definition, for a given pit depth, a smaller AR denotes a narrower pit. Fig. 6 illustrates schematically all different pit characteristics investigated in this study.

Based on the FEA of the intact joint as presented later, the most critical places in the flange and the web of the beam with higher equivalent plastic strain were identified and considered as submodels. Then, the isolated pit was moved in those areas according to predefined grids. For the tensile flange, the pit was assumed to penetrate the outer fiber of the flange by various location scenarios, as described in Fig. 7. This grid was defined above the weld access hole for the web of the beam, as illustrated in Fig. 8. The above-described pitting matrix includes 582 pitting scenarios which are different in terms of location, depth, and aspect ratio.

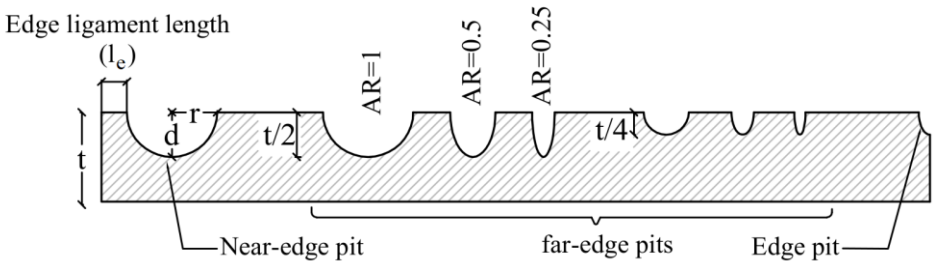

Fig. 6. An illustration of different investigated characteristics of the corrosion pit.

Table 1. Isolated pit characteristics matrix.

notation	pit depth (d)	location	pit aspect ratio (AR)	edge ligament length (l_e)
P1	$t/2$ *	far-edge	1	-
			0.5	-
			0.25	-
		near-edge	1	$t/12, t/6, t/4$
			0.5	$t/12, t/6, t/4$
			0.25	$t/12, t/6, t/4$
		edge	1	-
			0.5	-
			0.25	-
P2	$t/4$	far-edge	1	-
			0.5	-
			0.25	-
		near-edge	1	$t/12, t/6, t/4$
			0.5	$t/12, t/6, t/4$
			0.25	$t/12, t/6, t/4$
		edge	1	-
			0.5	-
			0.25	-
* t is 12.7mm for the flange plate and 8mm for the web plate.				

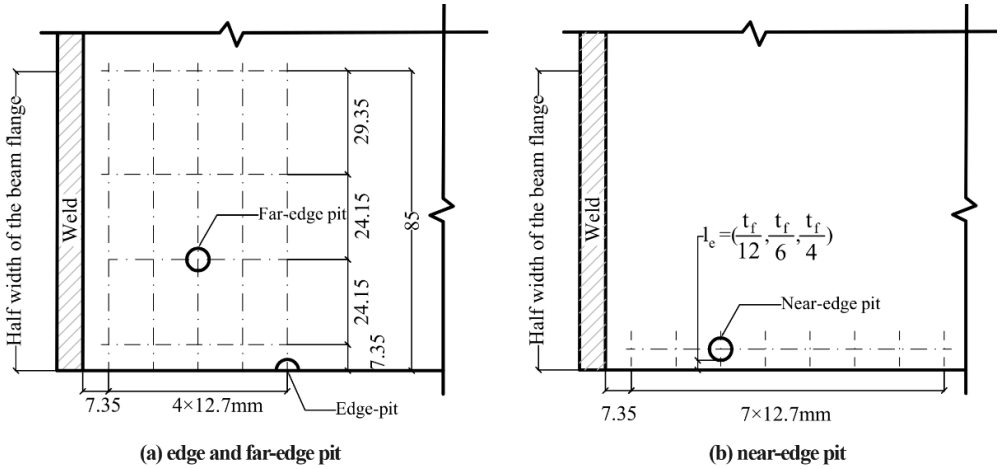

Fig. 7. Pit location grid on the flange of the beam (all dimensions are in mm).

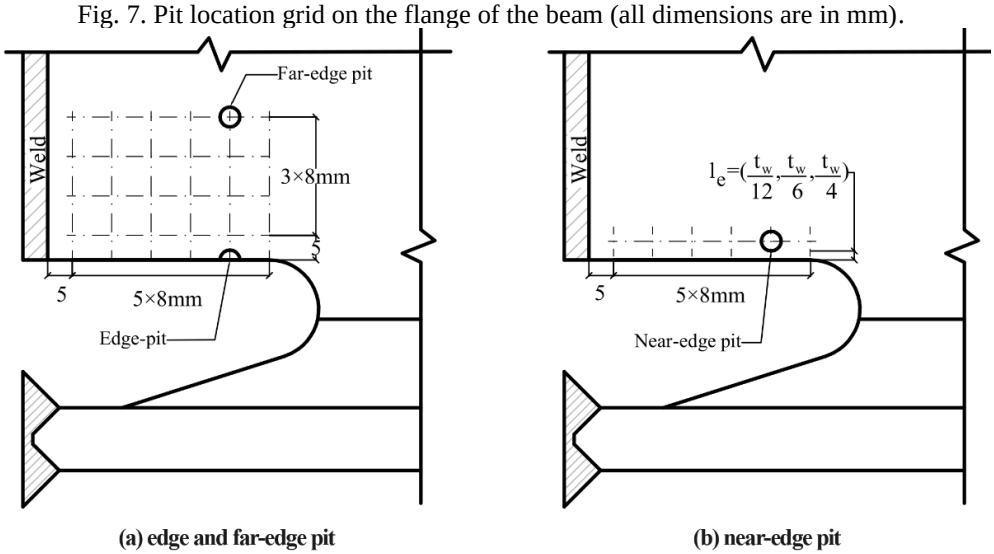

Fig. 8. Pit location grid on the web of the beam (all dimensions are in mm).

3.3. Finite element modeling

Abaqus finite element software was used based on an implicit integration scheme to simulate the global model and submodels. Eight-node brick elements with reduced integration (C3D8R) were used to discretize the geometry of models. This element is a general-purpose linear brick element with only one integration point at the center, significantly reducing computational time compared to fully integrated elements (Dassault Systèmes 2014). In addition, due to the reduced integration point, this element is not subjected to the shear locking phenomenon observed in fully integrated elements (Dassault Systèmes 2014).

Fig. 9 illustrates different mesh refinements used to discretize the geometry of the global model and submodels of the joint. To predict the fracture initiation in the intact submodel, a 1 mm mesh size was used (see Fig. 9.e). Previous studies (Kanvinde and Deierlein 2007; Mahdavipour and Vysochinskiy 2021) showed that elements larger than the material's characteristic length (ℓ^*) can predict fracture initiation accurately when there is no sharp notch. However, in submodels with corrosion pit, a very fine mesh (0.3-0.2 mm) was employed for the pits and surrounding areas, as shown in Fig. 9. This mesh size is approximately one-tenth of pit depth and is also comparable with the characteristic length of the mild steel (Kanvinde and Deierlein 2006; Liao et al. 2012). Similar mesh density was also used by (Wang et al. 2018). The other regions of the submodels were discretized by 3 mm mesh size as was used for the global model.

For the global model discretization, a 3 mm mesh density was employed at the critical region of the beam (near to the column face). The number of layers of elements through the thickness of plates in the global model was selected based on a standard mesh sensitivity analysis. For this purpose, the global model was analyzed for 3, 5, 7, and 9 layers of elements through the plates. Fig. 10.a compares the longitudinal nodal displacements across the beam flange where the boundary condition of the intact submodel was defined. These curves were obtained for 377 mm of joint vertical displacement corresponding to fracture initiation displacement of the intact submodel, as described later. According to these curves, nodal displacement in the global model changed only 0.21% in maximum when the number of layers increased from seven to nine. As a result, mesh refinement converged, and seven layers were selected to extract the submodels' boundary conditions.

To ensure that the mesh refinement in submodels did not change the stiffness significantly, the stress in the boundary of the intact submodel and global model are compared in Fig. 10.b. These curves were obtained for the same amount of joint vertical displacement (377 mm). This comparison indicated that the maximum difference between stress profiles in the submodel and global model is about 3%. This value implies that the boundary condition was transmitted from the global model to the submodel with an acceptable level of boundary condition error. Because of the symmetry of the sub-assemblage, only half geometry was modeled, and symmetric boundary condition was applied on the symmetry plane, as shown in Fig. 9. Boundary conditions were assigned to the Reference Points (RP) defined at the ends of the beam and the column. These reference points were constrained to the section nodes by kinematic coupling constraints. All these reference points were also restrained for out-of-plane movements. As shown in Fig. 9, the column removal was modeled by a static vertical displacement acting on *RP2*. It is important to realize that progressive collapse is a nonlinear dynamic phenomenon in nature. However, this study focused on capacity evaluation rather than demand assessment. Therefore, static push-down analysis was employed as a standard method recommended by reputable guidelines (GSA 2016) and (DoD 2009) that was also used in the recent open literature (Adam et al. 2018; Daneshvar and Driver 2019; Lee et al. 2021; Qian et al. 2020; Qiu et al. 2020; Wang et al. 2020).

The geometry of all welds was modeled to have realistic stress and strain distribution on the beam. All weld profiles were attached to the beam and column by tie constraints to simulate no relative motion between them (Dassault Systèmes 2014).

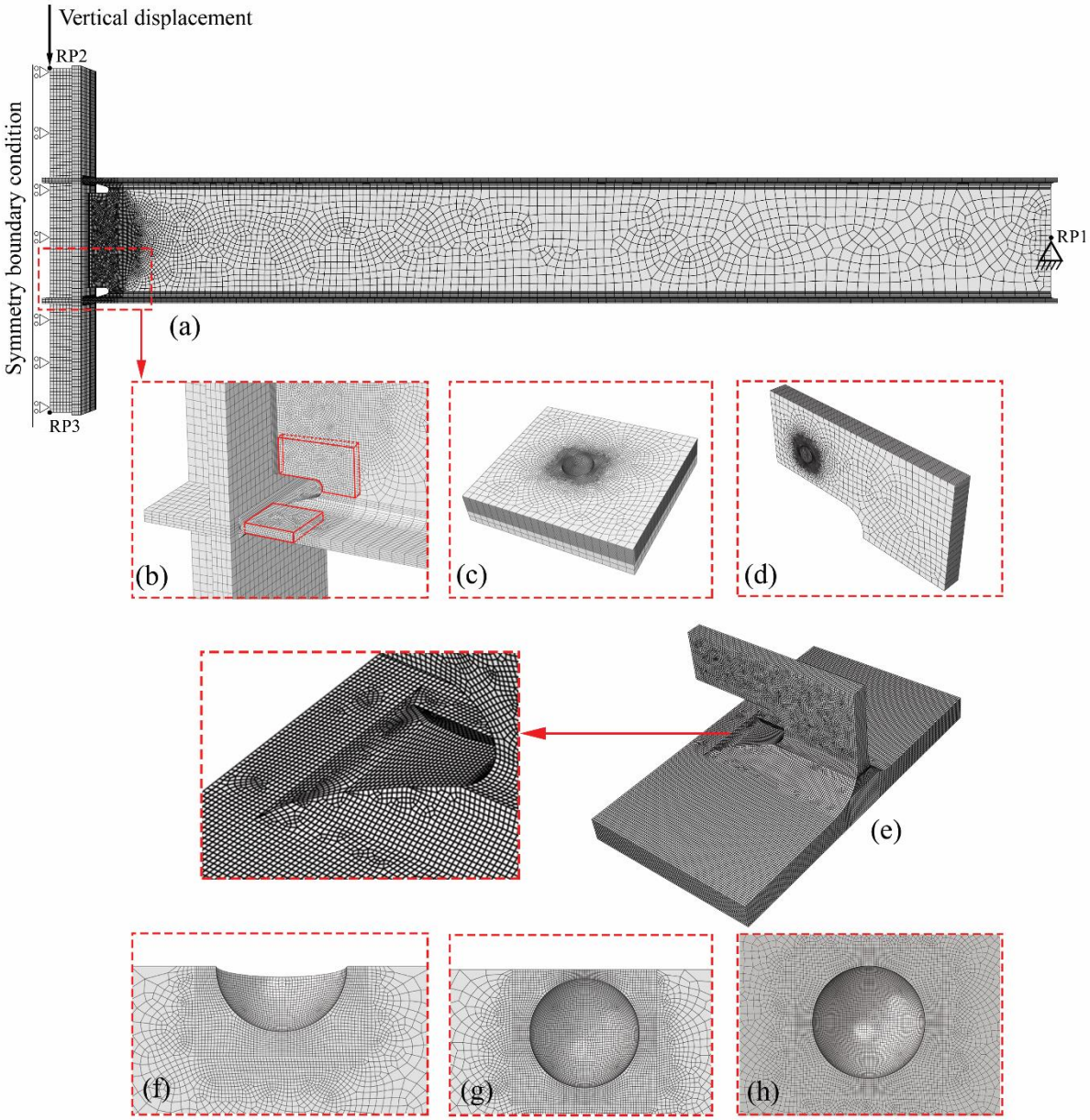

Fig. 9. Finite element modeling details: a) the global model of the joint and applied boundary conditions, b) mesh refinement in the global model, c) a submodel from the beam flange, d) a submodel from the beam web, e) Intact submodel and mesh configuration, f) mesh configuration of an edge pit, g) mesh configuration of a near-edge pit, h) mesh configuration of a far-edge pit.

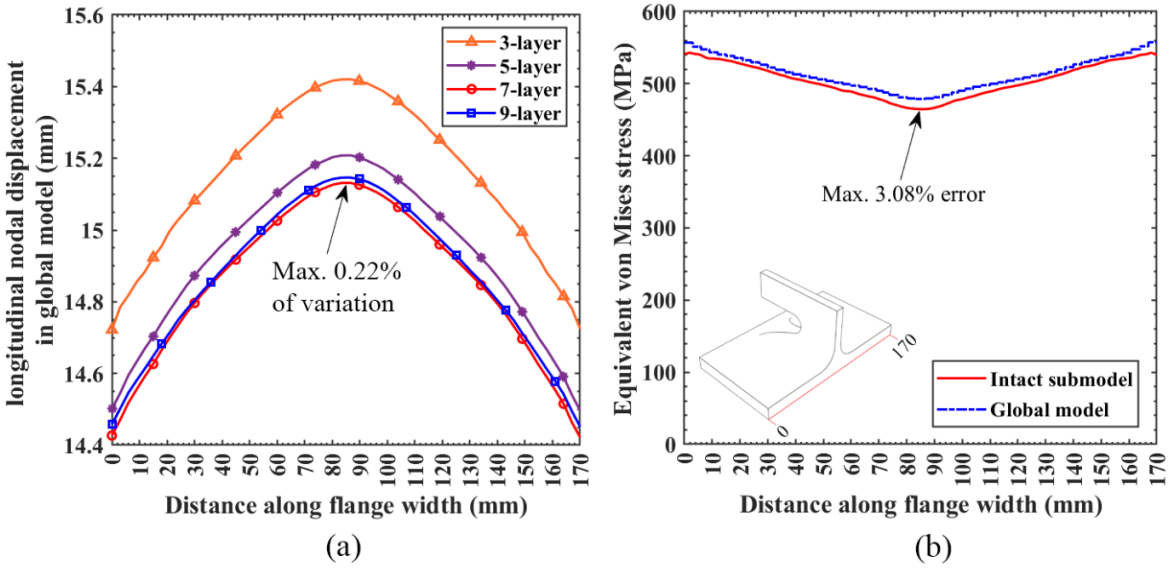

Fig. 10. Mesh sensitivity analysis result at the boundary of submodel region: a) Longitudinal nodal displacement of global model converged by using seven layers of elements through the thickness of the plates, b) Comparison between stress values obtained from the global model and submodel.

3.4. Calibrated material properties

Material nonlinear behavior of the joint was simulated by von Mises yield criterion associated with isotropic hardening. Fig. 11 illustrates the average plastic flow curves used for base metal (S355J2) calibrated by Mahdavipour and Vysochinskiy (2021). Calibrated $VGI_{critical}$ was also averaged 3.09 for this steel grade (Mahdavipour and Vysochinskiy 2021). The weld plastic flow curve adapted from (Tu 2017) is also shown in Fig. 11; however, the fracture of welds was not modeled. In addition, the average of Young's modulus (E) and Poisson's ratio (ν) was assumed to be 200 GPa and 0.3, respectively.

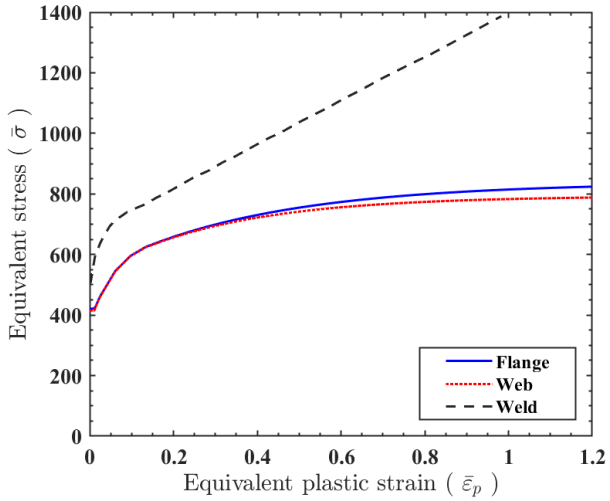

Fig. 11. Plastic flow curves used in the numerical models (Mahdavipour and Vysochinskiy 2021; Tu 2017).

Fig. 12 compares numerical and experimental force-displacement and fracture patterns of two pull-plate tests with different hole configurations (Mahdavipour and Vysochinskiy 2021). As this figure indicates, the above-described material model could predict the fracture of the tested specimens accurately. More information about these validation tests is available in (Mahdavipour and Vysochinskiy 2021).

It is worth mentioning that the VGM is not a built-in fracture criterion in Abaqus. Therefore, a USDFLD user subroutine was developed to implement the VGM in the numerical models. This subroutine was called at each time increment to calculate the VGI for all integration points.

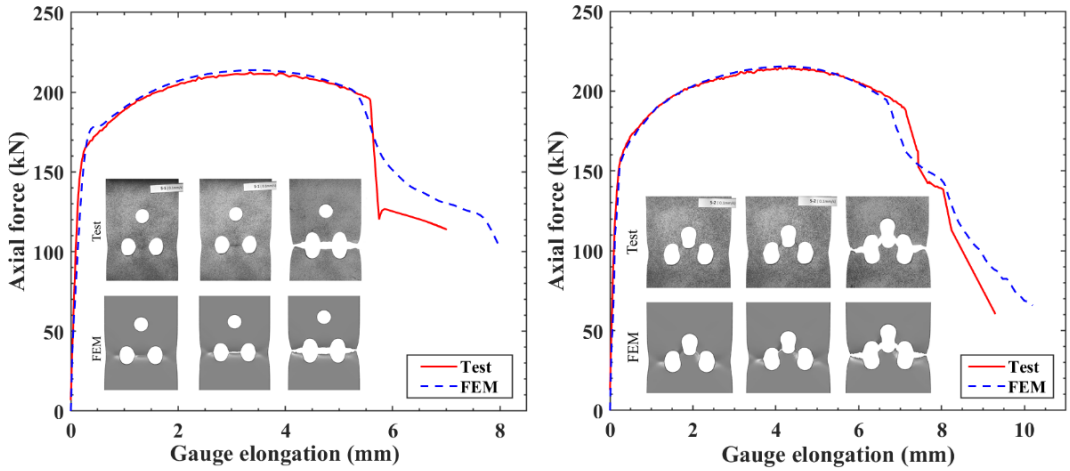

Fig. 12. Material model validation for two pull-plate specimens fabricated from S355J2 with different hole configurations (Mahdavipour and Vysochinskiy 2021).

4. Results and discussion

In this section, the joint vertical displacement corresponding to fracture initiation of the intact submodel (uncorroded) was considered as the benchmark value (hereafter is called fracture initiation displacement, $\Delta_{f(intact)}$). Then the corroded submodels with different described pit scenarios were investigated up to this displacement. Indeed, if a corrosion pit can initiate fracture by less vertical displacement of the joint, that is a deteriorating factor in terms of ductile fracture initiation.

4.1. Result of the intact joint

Fig. 13 shows the equivalent plastic strain ($\bar{\varepsilon}_p$) distribution and the fracture location predicted for the intact submodel. As indicated in this figure, the fracture occurred at the root of the weld access hole (center of the flange). The same pattern of fracture initiation was reported in similar types of joints studied by other

researchers (Sadek et al. 2010; Wang et al. 2021). Fig. 14 shows the vertical force-displacement curve of the intact joint up to the fracture initiation displacement ($\Delta_{f(intact)}$=377 mm). Beyond this displacement, the effect of the corrosion pit is less important because the intact joint is already fractured.

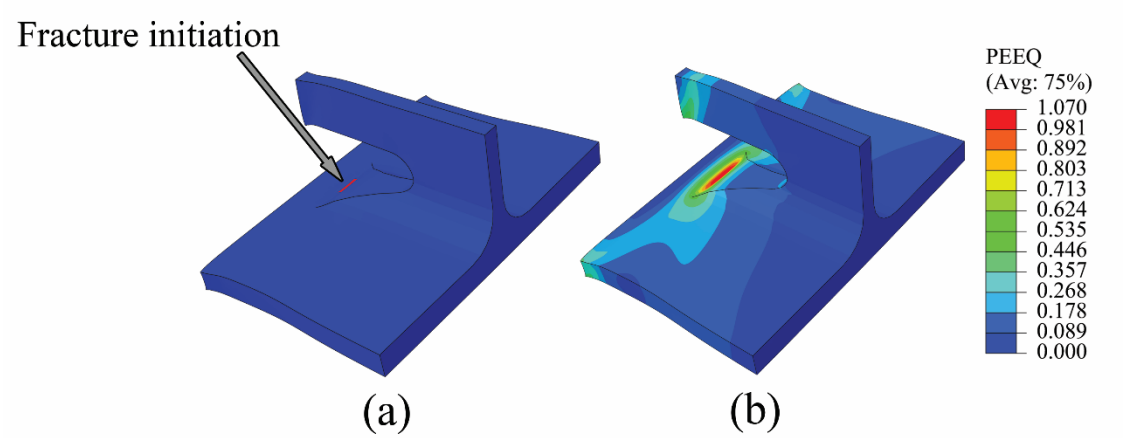

Fig. 13. Intact submodel to predict the fracture initiation of the uncorroded joint: a) mesh configuration b) location of fracture initiation, c) distribution of equivalent plastic strain ($\bar{\varepsilon}_p$).

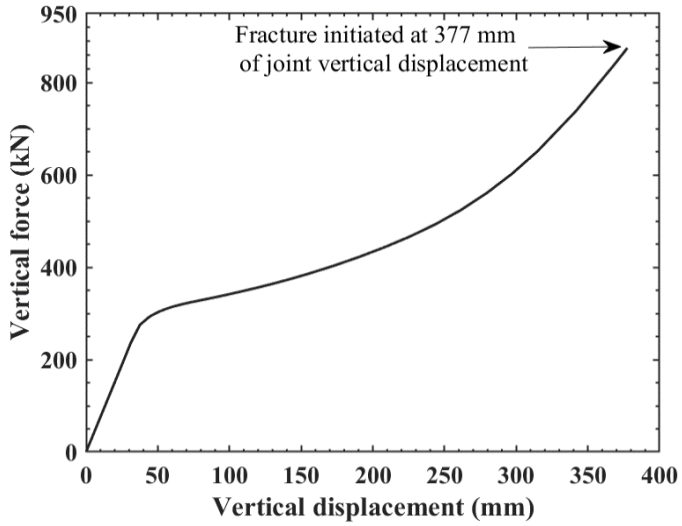

Fig. 14. The vertical force-displacement curve of the intact joint up to the fracture initiation displacement.

4.2. Result of the corroded joint

All submodels with an isolated corrosion pit were analyzed up to the fracture initiation displacement of the intact joint. Based on the results, dissimilar patterns of fracture initiation were observed in different pit categories. For the far-edge pits, the maximum VGI occurred at the root of the pits, and the ductile crack was initiated at this location. The near-edge pits fractured in the ligament between the pit and the free edge of the plates. The maximum VGI in the edge pits was observed on the wall; however, no fracture was observed for this pit category. Fig. 15 shows

examples of the VGI distribution and fracture initiation pattern of these three categories of pits.

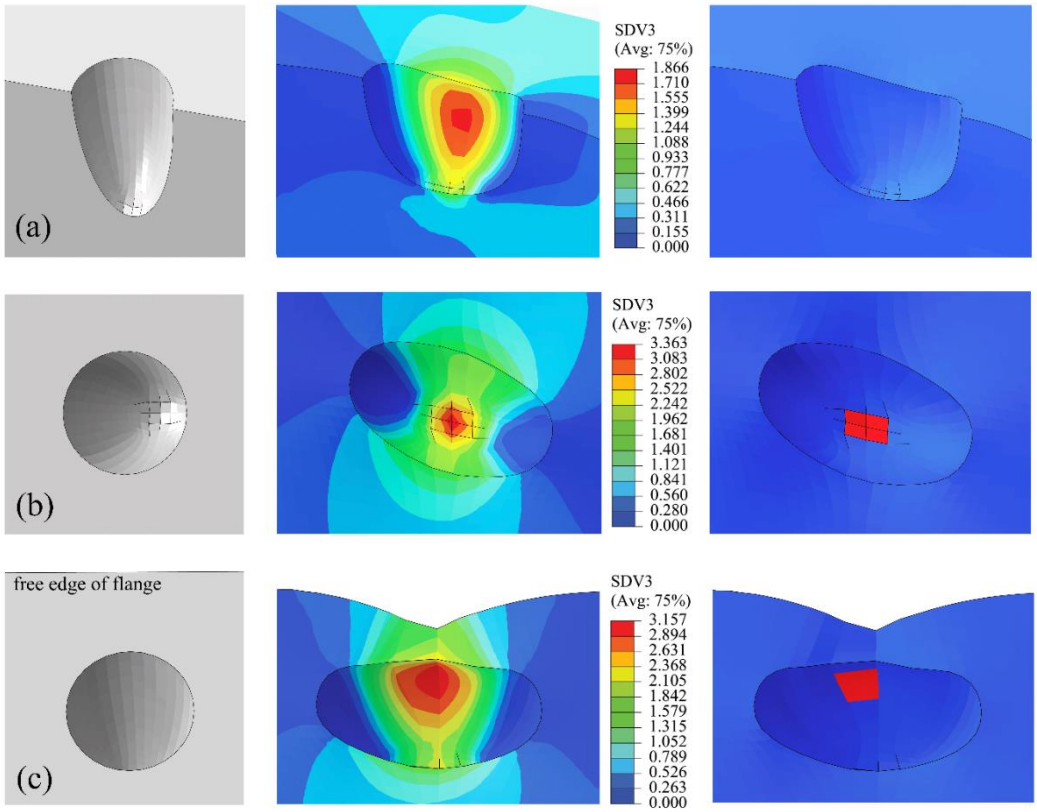

Figure 15. Examples of the VGI distribution and fracture initiation pattern: a) an edge pit without fracture initiation, b) a far-edge pit with fracture initiation at the root of the pit, c) a near-edge pit with fracture initiation at its ligament.

4.2.1.Edge and far-edge pits

Fig. 16 and 17 present the VGI ratio for the edge and far-edge pits in different locations. VGI ratio is defined as the maximum VGI normalized by $VGI_{critical}$. The VGI ratios larger than 1.0 are filled by gray color to denote locations with fracture initiation. Important to realize that ratios larger than 1.0 are physically impossible. However, in these figures, larger values were also used to make a more sensible comparison between different locations in terms of VGI demand. All these distributions of VGI ratio were obtained for a vertical displacement corresponding to the fracture initiation displacement of the intact joint ($\Delta_{f(intact)}$). According to these figures, the VGI ratio is lower than 1.0 for all free edges of the plates. It means that no edge pit was fractured before the intact joint fracture. As a result, such pits can be classified as noncritical pits for the fracture initiation of the joint. In contrast, the far-edge pits experienced VGI ratios larger the 1.0 in the region close to the butt welds and around the middle of the flange. Based on these distributions, no far-edge pit fractured in the distance larger than $2t_f$ from the

weld. For far-edge pits located on the web of the beam also a rectangular bounded by a distance less than $2t_w$ from the weld and about $3t_w$ from the weld access hole can be identified as the critical region. These values also indicate that the submodels were selected large enough to capture all critical places for fracture initiation of the pit. Fig. 16 and 17 also reveal more details about the effect of different pit geometrical characteristics (depth and aspect ratio). As a general trend, when the aspect ratio (AR) decreased, or the depth of pits (d) increased, the pits at the same location showed a higher VGI ratio. In other words, the gray areas which show the fractured state were larger for narrower and deeper pits (e.g., pits in the flange with $d = t_f/2$ and AR =0.25 were the most critical).

Although these figures are beneficial for identifying the critical locations with high potential of fracture initiation, they do not provide enough information about the reduction in the fracture initiation displacement of the joint. For this purpose, a scatter plot was drawn in Fig. 18 in which the ratio between fracture initiation displacement of the corroded joint and the intact joint ($\Delta_{f(corroded)}/\Delta_{f(intact)}$) is shown for all fractured far-edge pits. The points shown in this figure are classified based on the pit aspect ratio and location. Obviously, the pit fracture can reduce the fracture displacement of the joint by 11% in maximum; however, the average value for all fractured pits denotes less than 5% reduction that is negligible. Based on these ratios, one might conclude that edge and far-edge pits by the described characteristics would not affect the joint integrity significantly.

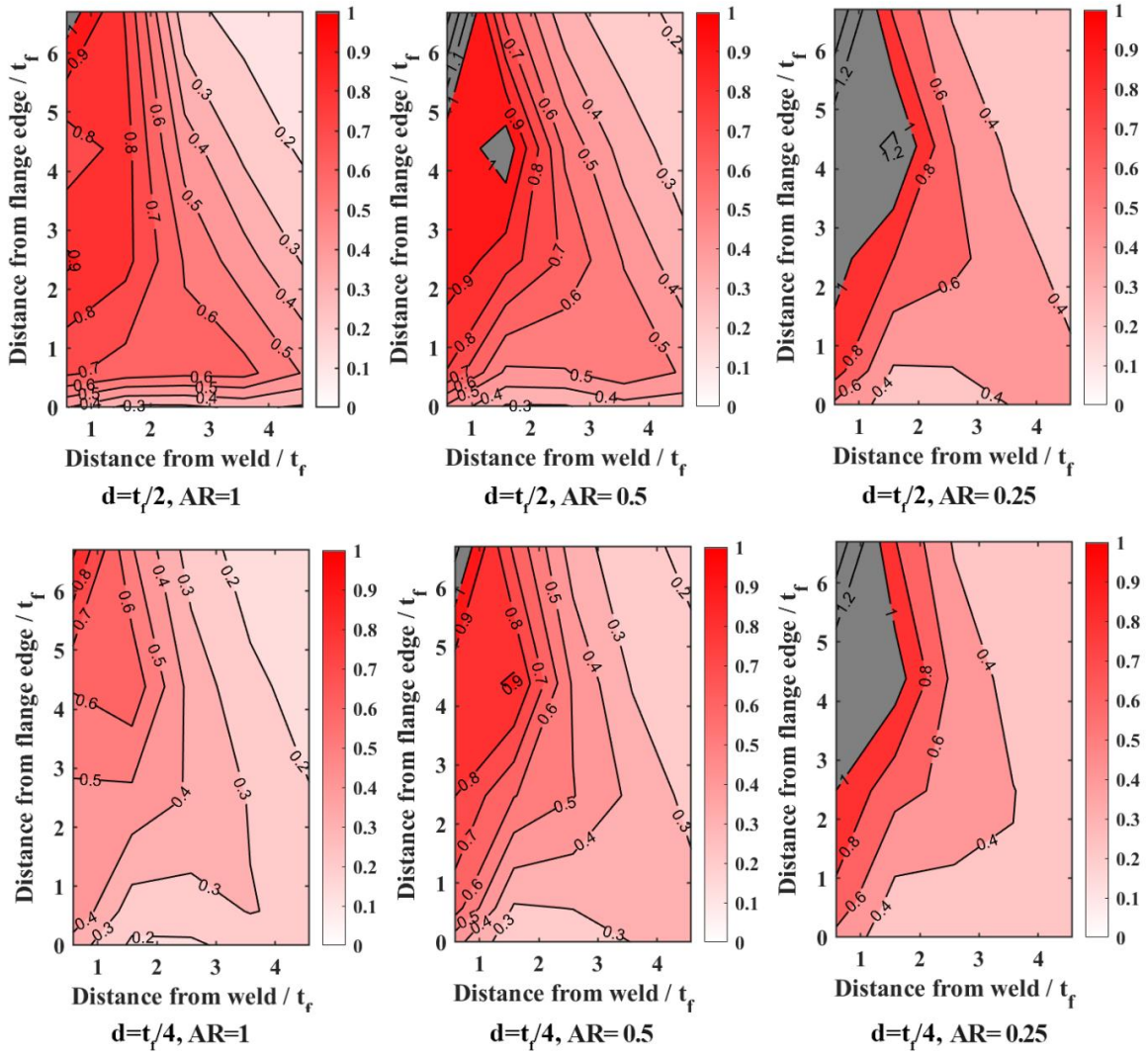

Figure 16. Distribution of the VGI ratio on the half flange of the beam for different depths and aspect ratios of the pit.

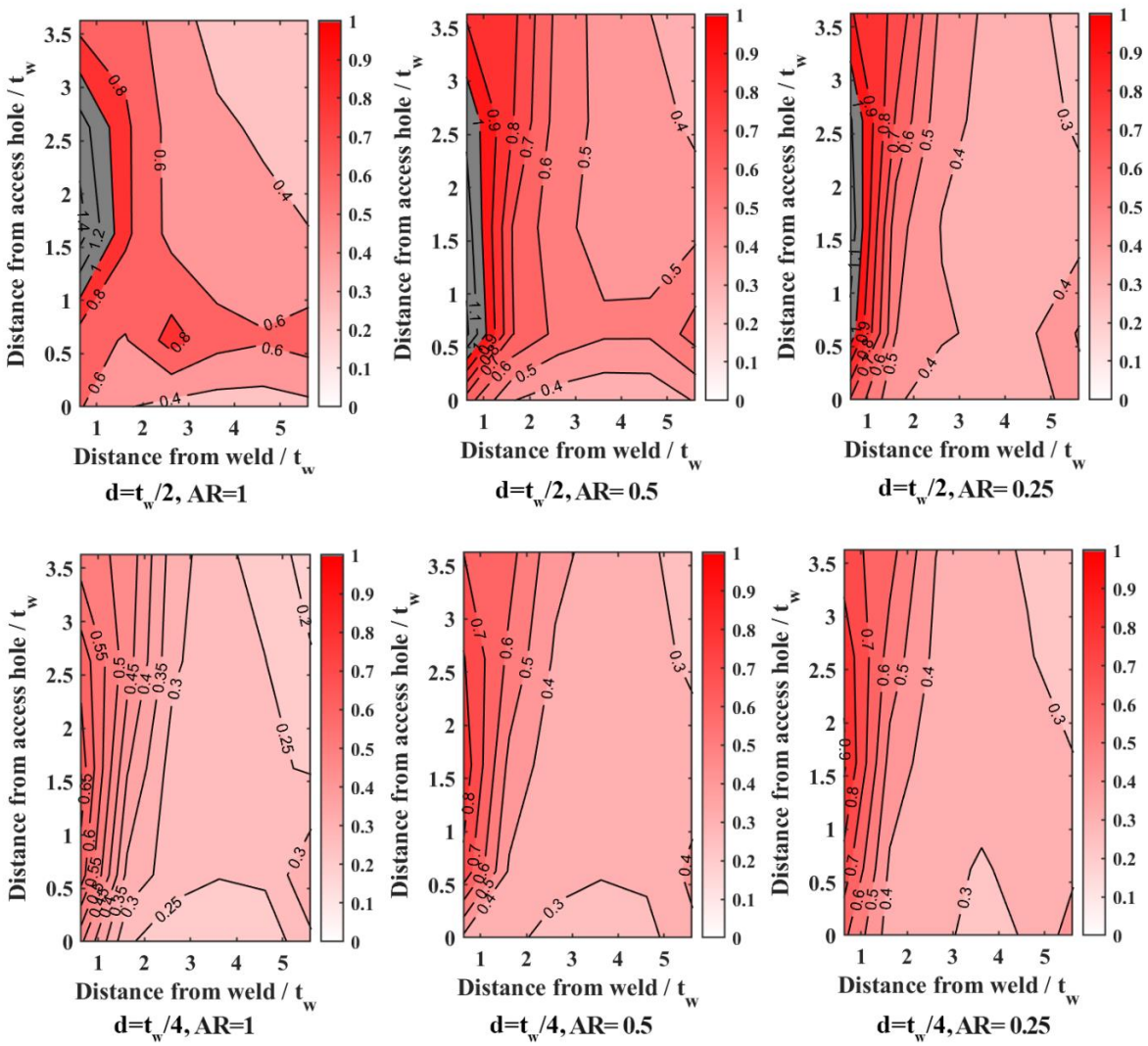

Figure 17. Distribution of the VGI ratio on the web of the beam for different depths and aspect ratios of the pit.

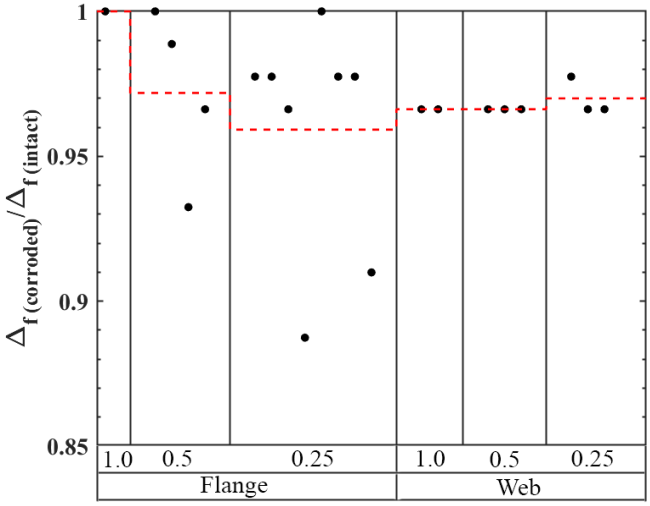

Figure 18. The ratio of fracture initiation displacement of the joint subjected to an isolated far-edge pit (the dashed line denotes the average ratio).

4.2.2.Near-edge pits

As described, the near-edge pits penetrate close to the free edge of the flange or weld access hole, and a ligament is formed between the pit and the edge of the plates (see Fig. 6). This ligament can act as a notch concentrating local stress and strain and starts ductile fracture when the joint sustains excessive plastic deformations. Fig. 19 shows the VGI ratio for the near-edge pits with $d = t_f/2$ and different aspect ratios (AR) and ligament lengths (l_e) as a portion of the flange thickness (t_f). The pits arrangement is shown in Fig. 7.b. The dashed lines in Fig. 19 indicate the fracture initiation threshold (VGI ratio=1). Based on this figure, one can determine a $7t_f$ (or equally about 0.25 of the beam depth) distance from the butt weld as a critical zone for the fracture initiation of the near-edge pits in the flange. In this zone, the fracture initiation in the ligaments could occur earlier than the fracture of the intact joint. However, it also depended on the ligament length (l_e). For example, almost all pits within this zone that also possessed a narrow ligament ($l_e = t_f/12$) experienced fracture before the intact joint while none of the pits with $l_e = t_f/4$ exceeded the fracture threshold. As this figure indicates, in general, a smaller AR increased the VGI ratio in the ligament but for some pits (e.g., pits with $l_e = t_f/12$) this rule is not the case. Indeed, the AR changes both the elevation and plan geometry of ligaments vice versa. Smaller AR (narrower pit) provides less metal between the pit wall and the flange edge while at the same time it increases the surrounding metal due to a smaller radius. The same results were obtained for the near-edge pits on the web of the beam as described in Fig. 8.b. Based on the results, the whole straight edge of the weld access hole was critical, and fracture initiated in most of the pits located in this region with a displacement smaller than the intact joint. To quantify the reduction in the fracture initiation displacement of the joint, a scatter plot of the ratio of fracture initiation displacement of the corroded joint and the intact joint ($\Delta_{f(corroded)}/\Delta_{f(intact)}$) is shown in Fig. 20 for all fractured near-edge pits. As this figure shows, the fracture was initiated with less than 75% of the joint vertical displacement for some near-edge pit scenarios. One may conclude if the initiated crack propagates as a ductile tearing and in the form of an unstable crack propagating could make a significant reduction (more than 25%) in the joint ductility. These results highlight the importance of inspection, monitoring, and treatment of such pits. It should be noted that increasing the pit size during the time of exposure can change a far-edge pit into a near-edge pit. More exposure time also can reduce the ligament of an

existing near-edge pit. Such a pit development near the edge of the plates would play a key role in the final ductility of the joint.

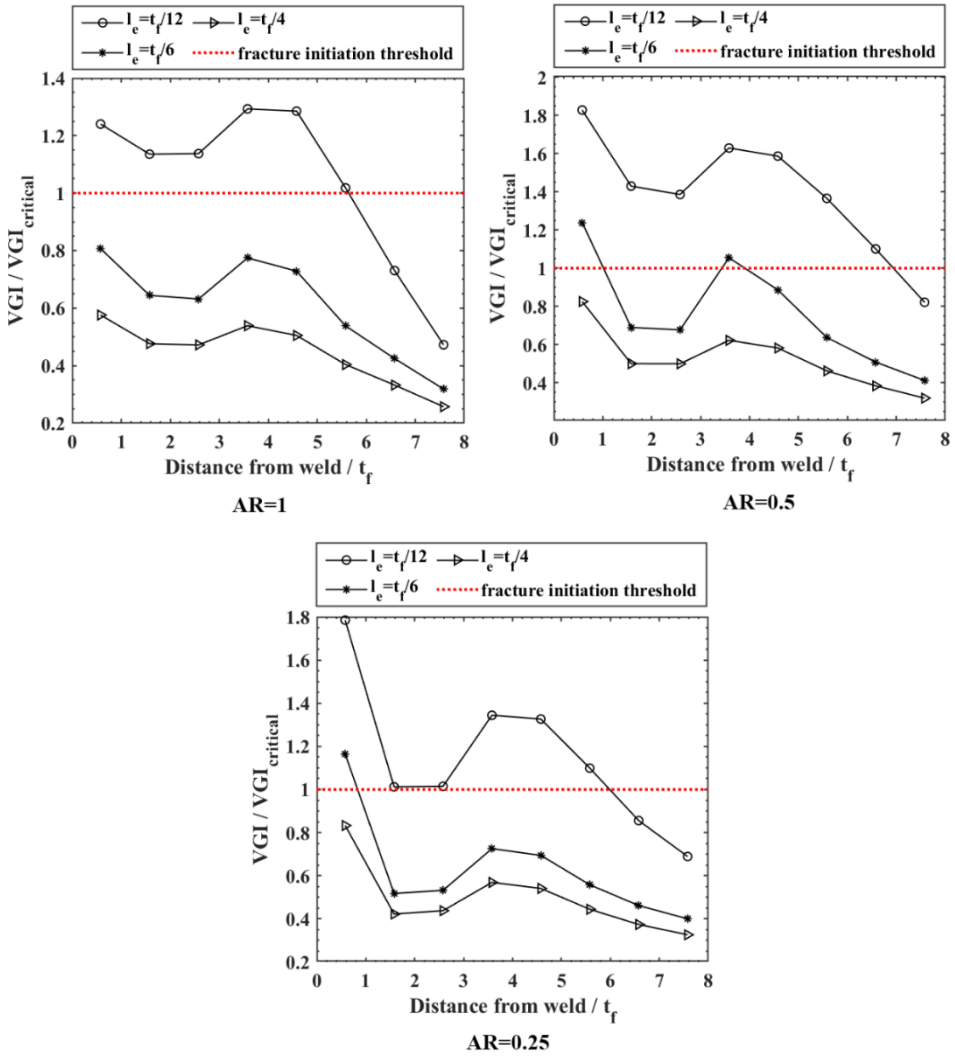

Figure 19. VGI ratio of the flange near-edge pits with $d = t_f/2$ (at the fracture initiation displacement of the intact joint).

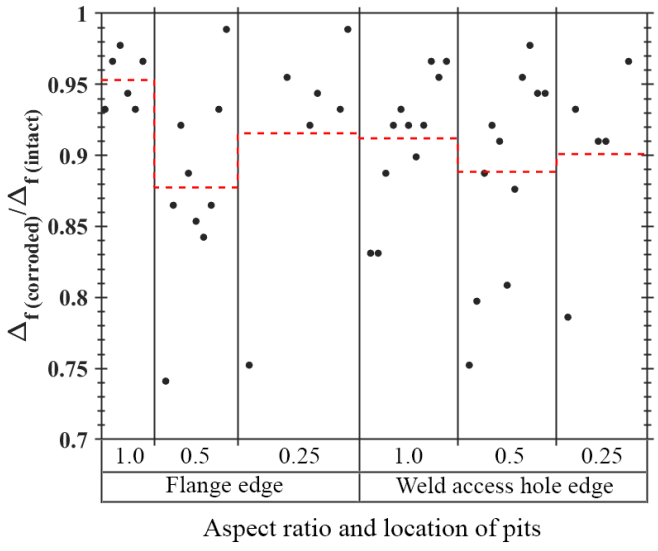

Figure 20. The fracture initiation displacement ratio of the joint subjected to an isolated near-edge pit (the dashed line denotes the average ratio).

5. Conclusions

Despite code requirements regarding protection methods to avoid pitting corrosion, it is still happening in steel structures located in aggressive environments. Furthermore, many aged facilities that are kept in operation beyond their design life can also be subjected to extreme events like a column removal scenario. In such a situation, the interaction between excessive plastic deformations and pitting localization can lead to ductility degradation by an accelerated fracture initiation. Therefore, evaluation of the pitting effect on the structural integrity of steel joints could be vital for the performance of the global structure under future events.

On the other hand, accurate numerical prediction of ductile fracture in corrosion pits requires a micromechanical fracture criterion and a fine three-dimensional solid mesh in the pit domain. However, for complicated geometry of beam-to-column joints implementing the pit geometry on the overall model of the joint and achieving proper mesh configuration is challenging and time-consuming.

In this study, two-level numerical modeling was employed to overcome these challenges. In this technique, a global model was used to carry out the nonlinear finite element analysis of the overall joint. Then various pit scenarios were investigated by micromechanical simulations on submodels taken from the critical regions of the joint.

This approach was examined through a parametric numerical study performed on a typical welded steel beam-to-column joint with an isolated corrosion pit and under a column removal scenario. The critical pitting scenarios were identified by comparing the fracture initiation of the corroded joint with the intact joint (uncorroded). Fracture initiation in the joint was studied for three categories of pits specified based on their location relative to the free edge of plates (edge, near-edge, and far-edge pits). Besides the location of the pit, the geometrical properties of the pit (depth and aspect ratio) were also investigated. For this purpose, two depths of pit penetration ($t/2$ and $t/4$) and three values of pit aspect ratio (1, 0.5, and 0.25), and also three values of edge ligament length ($t/12$, $t/6$, and $t/4$) were considered. In total, 582 submodels subjected to an isolated pit were analyzed. Based on the numerical outcomes of the case study joint, the main conclusions that can be drawn are:

- No edge pit was fractured before the intact joint fracture. As a result, such pits can be considered noncritical for the ductility of the joint.

- Far-edge pits close to the butt welds in both flange and web exhibited the fracture initiation earlier than the intact joint. However, the reduction in fracture displacement was minor (11% in maximum). As a result, such isolated pits also can be skipped due to their insignificant effect.
- Near-edge pits were identified as the most critical pits that can accelerate the fracture initiation of the joint compared to two other categories, particularly when they form a narrow ligament between the pit and the free edge of plates. The result showed that the fracture initiation displacement of the intact joint was reduced by about 25% when near-edge pits existed. If the initiated ductile crack propagates in the form of ductile tearing and unstable crack propagation, it can significantly reduce the joint ductility. These results highlight the importance of inspection, monitoring, and treatment of near-edge pits or far-edge pits that can change into a near-edge pit during the exposure time.
- Regarding geometrical parameters, the results showed that when the aspect ratio decreased (narrower pit) or the pit's depth increased, there was an increased tendency to fracture.

These results suggest the two-level numerical modeling as a capable technique to facilitate micromechanical simulation of pitting corrosion in complicated components under excessive plastic deformations. Based on this technique, engineers can scrutinize the behavior of corroded joints to find a proper treatment strategy.

6. Limitation and future work

This study is limited to an isolated pit. In a real situation, distribution of pits along with uniform corrosion can occur. As a result, the joint fracture behavior must also be investigated for a reduction of the cross-section area and interaction between pits. Future studies should consider a more realistic distribution of pits and involve more aspects of the problem, such as the joint size effect, structural details, and pitting corrosion of the welds. A procedure can be made to consider all these factors efficiently in the inspection, monitoring, and treatment of such joints to avoid their collapse for a prolonged lifetime.

7. References

Adam, J. M., Parisi, F., Sagaseta, J., and Lu, X. (2018). "Research and practice on progressive collapse and robustness of building structures in the 21st century." *Engineering Structures*, 173, 122-149.

Ahmmad, M. M., and Sumi, Y. (2010). "Strength and deformability of corroded steel plates under quasi-static tensile load." *Journal of marine science and technology*, 15(1), 1-15.

AISC (2016). "Prequalified connections for special and intermediate steel moment frames for seismic applications (AISC 358-16)." American Institute of Steel Construction, Chicago.

AISC (2016). "Seismic provisions for structural steel buildings (AISC 341-16)." American Institute of Steel Construction, Chicago.

American Welding Society (AWS) D1 Committee on Structural Welding (2016). "Structural welding code-seismic supplement (AWS D1.8/D1.8M:2016)." American Welding Society, MA.

Bardal, E. (2004). *Corrosion and protection*, Springer, London.

Cerit, M. (2013). "Numerical investigation on torsional stress concentration factor at the semi elliptical corrosion pit." *Corrosion Science*, 67, 225-232.

Cerit, M., Genel, K., and Eksi, S. (2009). "Numerical investigation on stress concentration of corrosion pit." *Engineering failure analysis*, 16(7), 2467-2472.

Chi, W.-M., Deierlein, G. G., and Ingraffea, A. (2000). "Fracture toughness demands in welded beam-column moment connections." *Journal of structural engineering*, 126(1), 88-97.

Cormier, N., Smallwood, B., Sinclair, G., and Meda, G. (1999). "Aggressive submodelling of stress concentrations." *International Journal for Numerical Methods in Engineering*, 46(6), 889-909.

Daneshvar, H., and Driver, R. G. (2019). "One-sided steel shear connections in progressive collapse scenario." *Journal of Architectural Engineering*, 25(2), 04019009.

Dassault Systèmes (2014). *ABAQUS Analysis User's Manual (Version 6.14)*, Dassault Systèmes Simulia Corp., Providence, RI.

DNV GL (2015). "Risk based corrosion management (DNVGL-RP-C302)." DNV GL AS.

DoD (2009). "Design of buildings to resist progressive collapse (UFC 4-023-03)." Department of Defence,, Washington, DC.

Duddu, R. (2014). "Numerical modeling of corrosion pit propagation using the combined extended finite element and level set method." *Computational Mechanics*, 54(3), 613-627.

European Committee for Standardization (2004). "Standard for hot-rolled structural steel. Part 2 - Technical delivery conditions for non-alloy structural steels (EN 10025-2:2004).", CEN, Brussels, Belgium.

GSA (2016). "Alternate path analysis & design guidelines for progressive collapse resistance." General Services Administration.

Hirai, I., Wang, B. P., and Pilkey, W. D. (1984). "An efficient zooming method for finite element analysis." *International Journal for Numerical Methods in Engineering*, 20(9), 1671-1683.

Huang, Y., Zhang, Y., Liu, G., and Zhang, Q. (2010). "Ultimate strength assessment of hull structural plate with pitting corrosion damnification under biaxial compression." *Ocean Engineering*, 37(17-18), 1503-1512.

International Standards Organization (2008). "Petroleum and natural gas industries-fixed steel offshore structures, ISO 19902." International Organization for Standardization.

Ji, J., Zhang, C., Kodikara, J., and Yang, S.-Q. (2015). "Prediction of stress concentration factor of corrosion pits on buried pipes by least squares support vector machine." *Engineering Failure Analysis*, 55, 131-138.

Jia, L.-J., and Ge, H. (2019). *Ultra-low-Cycle Fatigue Failure of Metal Structures Under Strong Earthquakes*, Springer.

Kanvinde, A., and Deierlein, G. (2004). "Micromechanical simulation of earthquake-induced fracture in structural steel." *Rep. No.145*, The John A. Blume Earthquake Engineering Center, Stanford.

Kanvinde, A., and Deierlein, G. (2006). "The void growth model and the stress modified critical strain model to predict ductile fracture in structural steels." *Journal of Structural Engineering*, 132(12), 1907-1918.

Kanvinde, A., and Deierlein, G. (2007). "Finite-element simulation of ductile fracture in reduced section pull-plates using micromechanics-based fracture models." *Journal of Structural Engineering*, 133(5), 656-664.

Kardak, A. A. (2015). "On an effective submodeling procedure for stresses determined with finite element analysis." Doctorate of Philosophy, Louisiana State University.

Lee, S.-Y., Noh, S.-Y., and Lee, D. (2021). "Comparison of progressive collapse resistance capacities of steel ordinary and intermediate moment frames considering different connection details." *Engineering Structures*, 231, 111753.

Lew, H. S., Main, J. A., Robert, S. D., Sadek, F., and Chiarito, V. P. (2013). "Performance of steel moment connections under a column removal scenario. I: Experiments." *Journal of Structural Engineering*, 139(1), 98-107.

Liao, F., Wang, W., and Chen, Y. (2012). "Parameter calibrations and application of micromechanical fracture models of structural steels." *Structural engineering and mechanics*, 42(2), 153-174.

Liu, J., Liu, Y., Liu, L., Yu, Y., and He, X. (2021). "Submodeling method to study the residual stress of TBCs near the interfacial asperity on a vane." *Engineering Failure Analysis*, 122, 105220.

Mahdavipour, M. A., and Vysochinskiy, D. (2021). "Using a DIC-based approach to enhance the calibration accuracy of the void growth model ductile fracture criterion." Unpublished manuscript,University of Agder

Mao, K., and Sun, C. (1991). "A refined global-local finite element analysis method." *International journal for numerical methods in engineering*, 32(1), 29-43.

Mao, K., and Sun, C. (1992). "Error estimators using global–local methods." *International Journal for numerical methods in Engineering*, 35(3), 589-599.

Marenić, E., Skozrit, I., and Tonković, Z. (2010). "On the calculation of stress intensity factors and J-integrals using the submodeling technique." *Journal of pressure vessel technology*, 132(4).

McClintock, F. A. (1968). "A criterion for ductile fracture by the growth of holes." *Journal of applied mechanics*, 35(2), 363-371.

Mora, D., Garrido, O. C., Mukin, R., and Niffenegger, M. (2020). "Fracture mechanics analyses of a reactor pressure vessel under non-uniform cooling with a combined TRACE-XFEM approach." *Engineering Fracture Mechanics*, 238, 107258.

Narvydas, E., and Puodziuniene, N. "Applications of sub-modeling in structural mechanics." *Proc., Proceedings of 19th International Conference. Mechanika, Kaunas, Lithuania*, 172-176.

Oñate, E. (2013). *Structural analysis with the finite element method. Linear statics: volume 2: beams, plates and shells*, Springer Science & Business Media.

Pedeferri, P. (2018). *Corrosion Science and Engineering*, Springer, Switzerland.

Petti, J. P., and Dodds Jr, R. H. (2005). "Ductile tearing and discrete void effects on cleavage fracture under small-scale yielding conditions." *International Journal of Solids and Structures*, 42(13), 3655-3676.

Pidaparti, R. M., and Patel, R. R. (2008). "Correlation between corrosion pits and stresses in Al alloys." *Materials Letters*, 62(30), 4497-4499.

Qian, K., Lan, X., Li, Z., Li, Y., and Fu, F. (2020). "Progressive collapse resistance of two-storey seismic configured steel sub-frames using welded connections." *Journal of Constructional Steel Research*, 170, 106117.

Qiu, L., Lin, F., and Wu, K. (2020). "Improving progressive collapse resistance of RC beam–column subassemblages using external steel cables." *Journal of Performance of Constructed Facilities*, 34(1), 04019079.

Rice, J. R., and Tracey, D. M. (1969). "On the ductile enlargement of voids in triaxial stress fields." *Journal of the Mechanics and Physics of Solids*, 17(3), 201-217.

Sadek, F., Main, J. A., Lew, H. S., Robert, S. D., Chiarito, V. P., and El-Tawil, S. (2010). "An experimental and computational study of steel moment connections under a column removal scenario." *NIST Technical Note*, 1669.

Songbo, R., Ying, G., Chao, K., Song, G., Shanhua, X., and Liqiong, Y. (2021). "Effects of the corrosion pitting parameters on the mechanical properties of corroded steel." *Construction and Building Materials*, 272, 121941.

Sun, C., and Mao, K. (1988). "A global-local finite element method suitable for parallel computations." *Computers & structures*, 29(2), 309-315.

Tu, H. (2017). *Numerical simulation and experimental investigation of the fracture behaviour of an electron beam welded steel joint*, Springer.

Turnbull, A., Wright, L., and Crocker, L. (2010). "New insight into the pit-to-crack transition from finite element analysis of the stress and strain distribution around a corrosion pit." *Corrosion Science*, 52(4), 1492-1498.

Verma, A. S., Vedvik, N. P., Haselbach, P. U., Gao, Z., and Jiang, Z. (2019). "Comparison of numerical modelling techniques for impact investigation on a wind turbine blade." *Composite Structures*, 209, 856-878.

Wang, F., Yang, J., and Pan, Z. (2020). "Progressive collapse behaviour of steel framed substructures with various beam-column connections." *Engineering Failure Analysis*, 109, 104399.

Wang, H., Huo, J., Liu, Y., Wang, N., and Elchalakani, M. "Experimental and numerical study on impact behavior of beam-column substructures of steel frame." *Proc., Structures*, Elsevier, 14-29.

Wang, H., Xu, S., Wang, Y., and Li, A. (2018). "Effect of pitting degradation on ductile fracture initiation of steel butt-welded joints." *Journal of Constructional Steel Research*, 148, 436-449.

Wang, Y., Xu, S., Wang, H., and Li, A. (2017). "Predicting the residual strength and deformability of corroded steel plate based on the corrosion morphology." *Construction and Building Materials*, 152, 777-793.

Wang, Y., Zhou, H., Shi, Y., and Xiong, J. (2011). "Fracture prediction of welded steel connections using traditional fracture mechanics and calibrated micromechanics based models." *International Journal of Steel Structures*, 11(3), 351.

Xu, S., Wang, H., Li, A., Wang, Y., and Su, L. (2016). "Effects of corrosion on surface characterization and mechanical properties of butt-welded joints." *Journal of Constructional Steel Research*, 126, 50-62.

Yan, Y., Shao, B., Zhou, X., Song, S., Zhou, X., and Yan, X. (2019). "A study on the influence of double ellipsoidal pitting corrosion on the collapsing strength of the casing." *Engineering Failure Analysis*, 100, 11-24.

Zhang, J., Liang, Z., and Han, C. (2015). "Effects of ellipsoidal corrosion defects on failure pressure of corroded pipelines based on finite element analysis." *International Journal of Electrochemical Science*, 10, 5036-5047.

Zhao, Z., Zhang, H., Xian, L., and Liu, H. (2020). "Tensile strength of Q345 steel with random pitting corrosion based on numerical analysis." *Thin-Walled Structures*, 148, 106579.